The far distance to G7.47+0.06 from proper motion measurement of H₂O masers

Aya Yamauchi,[1,*,†] **Kazuyoshi Yamashita,**[1] **Mareki Honma,**[1] **Kazuyoshi Sunada,**[1] **Akiharu Nakagawa,**[2] **and Yuji Ueno**[1]

[1]Mizusawa VLBI Observatory, National Astronomical Observatory of Japan, 2-12 Hoshigaoka, Mizusawa-ku, Oshu, Iwate 023-0861, Japan

[2]Graduate School of Science and Engineering, Kagoshima University, 1-21-35 Korimoto, Kagoshima, Kagoshima 890-0065, Japan

*E-mail: a.yamauchi@nao.ac.jp

†Research Fellow, Japan Society for the Promotion of Science

Abstract

We report on a distance measurement of 22 GHz H₂O maser features associated with an ultra-compact H II region G7.47+0.06 using VERA (VLBI Exploration of Radio Astrometry). Since the source is located farther away than 10 kpc, it turned out to be difficult to derive the distance from annual parallax measurement. Meanwhile, we clearly detected the source's proper motion parallel to the Galactic plane. The proper motion is $\mu = -5.03 \pm 0.07\,\mathrm{mas\,yr^{-1}}$ and is approaching the Galactic center. We applied a new method to determine the source distance based on absolute proper motions. Considering uncertainties of the Galactic rotation curve and the solar peculiar motion, the detected proper motion leads to a source distance of $D = 20 \pm 2\,\mathrm{kpc}$, demonstrating that astrometric observation can provide an accurate distance measurement at a 10% level even for sources too distant to measure the annual parallax. Lastly, we scale the physical parameters of the H II region estimated in a previous paper to be 20 kpc, and show that the H₂O maser features are associated with a massive star-forming region corresponding to the spectral type of O5.5.

Key words: Galaxy: kinematics and dynamics — masers — stars: individual (G7.47+0.06)

1 Introduction

Very Long Baseline Interferometry (VLBI) astrometry allows us to directly measure the distances and proper motion of Galactic maser sources. By combining parallax and proper motion with the coordinates on the sky and the radial velocity, we are able to obtain the three-dimensional position and velocity of the sources in the Galaxy. Using these VLBI astrometric results, Galactic structure and dynamics such as the spiral arm and Galactic rotation have been studied (e.g. Honma et al. 2012; Reid et al. 2014).

Recent VLBI astrometric observations, such as the VLBI Exploration of Radio Astrometry (VERA) project (Honma et al. 2000; Kobayashi et al. 2008) and the Bar and Spiral Structure Legacy Survey, have yielded over 100 trigonometric parallax measurements with accuracies of typically about $\pm 20\,\mu$as, and some as good as $\pm 5\,\mu$as (Reid et al. 2014). The target accuracy of VERA, 10 μas level, allows us

Table 1. VERA observations of G7.47+0.06.[†]

| Date | DOY | $\theta_{maj} \times \theta_{min}$ (PA) | T^*_{sys} [K] | | | | Calib. |
		[mas × mas (°)]	MIZ	IRK	OGA	ISG	for B[‡]
2009 Mar 03	2009/062	3.47 × 1.69 (162.4)	180–730	180–380	180–610	220–390	J
2009 May 16	2009/136	2.78 × 1.46 (152.3)	200–12300	180–950	250–2970	230–2120	J
2009 Aug 27	2009/239	3.52 × 1.64 (159.8)	260–12650	210–1330	220–4370	260–2570	J
2010 Jan 09	2010/009	4.43 × 1.75 (156.2)	120–570	120–340	120–3790	180–3930	J
2010 May 09	2010/068	3.02 × 1.52 (157.9)	170–2940	110–1680	230–12670	190–1010	J
2010 May 31	2010/151	4.50 × 1.93 (171.9)	–	220–800	210–600	250–1690	J
2010 Oct 24	2010/297	2.83 × 1.45 (154.1)	220–2510	370–12670	300–12810	340–2350	J
2010 Dec 22	2010/356	3.05 × 1.50 (152.3)	120–950	100–270	140–3030	150–450	N
2011 May 08	2011/128	2.92 × 1.46 (152.3)	110–830	310–2500	240–5390	300–2620	N,B
2011 Sep 12	2011/255	2.95 × 1.54 (156.4)	230–5880	170–890	250–12810	330–12130	M,B
2011 Dec 21	2011/355	5.37 × 0.69 (134.6)	110–720	110–710	140–6820	220–1070	M,B

[†]NRA O 530, BL Lac, and M 87 are the sources of the Gamma-ray Emitting Notable AGN Monitoring by Japanese VLBI (GENJI) programme, which started in 2010 November (Nagai et al. 2013). GENJI observations use the time for observing bright calibrators in VERA project observations. The observing coordinates of 1733−1304 are slightly different (<0.1 mas) from those of NRA O 530, although J1733−1304 is an alias of NRA O 530.

[‡]Bandpass and delay calibration sources for B-beam. J: J1733−1304; N: NRA O 530; B: BL Lac; M: M 87.

to determine the distance on the 1–10 kpc scale with errors of less than 10%. It is usually difficult to accurately ($\approx 10\%$) measure the parallax of an object at a distance of over 10 kpc. In particular, no parallax of an object beyond the Galactic center (its galactic longitude $l \approx 0°$) has been measured: since most VLBI arrays including VERA are located in the Northern Hemisphere, the low elevation of the object near the Galactic center makes its accurate parallax measurement difficult.

Recently, Sofue (2011) discussed the accuracy of methods used for determining kinematical distances from radial velocities and proper motions. Given a rotation curve, and assuming the circular motion of an object, the distance to the object is obtained from not only the radial velocity but also the proper motion, kinematically. In the proper-motion method, the distance ambiguity is drastically reduced in the region beyond the Galactic center near the line passing through the Sun and the Galactic center (the Sun–GC line). Sofue (2011) tried to measure distances of two near objects whose parallaxes have already been obtained. Here, we apply this method to a far object, G7.47+0.06. G7.47+0.06 is suitable for measuring distance using proper motion rather than radial velocity because it is located beyond the Galactic center.

G7.47+0.06 is an ultra-compact (UC) H II region associated with IRAS 17591−2228. The systemic velocity (v_{sys}) is −13.9 km s^{-1}, which was obtained by CS(2–1) observations of the IRAS source (Bronfman et al. 1996). The H$_2$O maser source (6_{16}–5_{23}, 22235.080 MHz) in G7.47+0.06 is listed in the Arcetri atlas (Comoretto et al. 1990). The peak feature at a velocity of −16.6 km s^{-1} has a flux density of $S = 10.7$ Jy.

Although the trigonometric and spectrophotometric distances to this source were not measured, some kinematic distances were derived from the radial velocities of radio hydrogen recombination lines and molecular emission lines. The sources in the inner solar circle have two possible kinematic distances corresponding to measured velocity, namely "near" and "far." Peeters et al. (2002) reported 3.0 and 13.8 kpc to be near and far distances of G7.47+0.06, respectively. In many cases, the velocities of some molecular absorption lines toward G7.47+0.06 support the far distance (e.g., 27 ± 5 kpc, Downes et al. 1980; $25.1^{+10.8}_{-4.2}$ kpc, Wink et al. 1982).[1] These kinematic distances suggest that G7.47+0.06 may be farther away than the distance between the Galactic center and the Sun.

In this paper, we first adopt the proper-motion method proposed by Sofue (2011) for the possible distant object G7.47+0.06. Based on monitoring observations of the H$_2$O maser source with VERA, we measure the proper motions and obtain its distance using the proper-motion method. Throughout this paper, we adopt velocities in the radio definition and with respect to the local standard of rest (LSR).

2 VLBI observations with VERA

Observations of the 22 GHz H$_2$O maser line associated with G7.47+0.06 were conducted with VERA from 2009 March to 2011 December. We present the results from a total of 11 observing epochs listed in table 1; hereafter, an observing epoch is denoted by "year/day of the year"

[1] Downes et al. (1980) and Wink, Altenhoff, and Mezger (1982) adopt $R_0 = 10$ kpc as the distance between the Galactic center and the LSR. Peeters et al. (2002) uses $R_0 = 8.5$ kpc.

(DOY). All four VERA stations, Mizusawa (MIZ), Iriki (IRK), Ogasawara (OGA), and Ishigaki-jima (ISG), providing a maximum baseline length of 2270 km, participated at 10 epochs, but only three (IRK, OGA, and ISG; see figure 1 of Petrov et al. 2007) participated in the 2010/151 epoch.

Observations were made in the dual-beam mode (Kawaguchi et al. 2000; Honma et al. 2008), and we simultaneously observed the H_2O maser source in G7.47+0.06 ($\alpha_{J2000.0} = 18^h 02^m 13^s.179$, $\delta_{J2000.0} = -22°27'58''.96$, which corresponds to $l = 7°.47065$, $b = 0°.05845$) and a reference source, J1755−2232 ($\alpha_{J2000.0} = 17^h 55^m 26^s.2847840$, $\delta_{J2000.0} = -22°32'10''.616510$). The separation angle between those two sources was $1°.57$. Left-handed circular polarization was received at receivers and sampled with 2-bit quantization and was filtered using the VERA digital filter unit (Iguchi et al. 2005). The data were recorded on to magnetic tapes at a rate of 1024 Mbps, providing a total bandwidth of 256 MHz. The bandwidth was divided into 16 IF channels (16 MHz each). One IF was assigned to G7.47+0.06 (A-beam), and the other 15 IFs were assigned to J1755−2232 (B-beam). J1755−2232 was detected with a peak intensity ranging from ∼95 to 435 mJy beam^{-1} throughout all the epochs; the signal-to-noise ratio (SNR) was 48–153. Bright continuum sources were also observed every 90 min as bandpass and delay calibrators; we observed J1733−1304 throughout all the epochs in A-beam. The observed sources in B-beam, J1733−1304, NRA O 530, BL Lac, and M 87, are different at each epoch.

Table 1 shows synthesized beam sizes (major and minor axes), their position angle, system noise temperature of each station (T_{sys}^*), and calibration sources for B-beam at all the epochs. T_{sys}^*, including atmospheric attenuation, depended on weather conditions and also on the elevation angle of the observed sources. Correlation processing was carried out on the Mitaka FX correlator (Chikada et al. 1991) located on the NAOJ Mitaka campus. The spectral resolutions of the H_2O maser line were set at 15.625 kHz on 2009/136, 2009/239, and 2010/009 epochs, and 31.25 kHz on the other epochs. These spectral resolutions correspond to velocity resolutions of 0.21 km s^{-1} and 0.42 km s^{-1}, respectively.

3 Data reduction with VEDA

We conducted the data reduction with the VERA Data Analyzer (VEDA) software package. VEDA was developed for astrometric analysis of data observed with the VERA dual-beam system by the software development group at the National Astronomical Observatory of Japan's (NAOJ) Mizusawa VLBI Observatory.

At first we took time and frequency averages of the data on the position reference source J1755−2232 to reduce the data size; thus, the integrated time and frequency are 4 s and 1 MHz, respectively. We also took the time average (4 s) of the data of the maser source G7.47+0.06. After averaging, we carried out amplitude and bandpass calibrations on G7.47+0.06 and J1755−2232 independently. Amplitude calibrations were performed based on the T_{sys}^* data monitored during the scans. The bandpass calibrations were performed using autocorrelation spectra of the blank-sky data and the bright calibrator sources (J1733−1304, and so on).

A fringe search was first conducted using the visibility data of the fringe-finder (J1733−1304, and so on) to determine the delay and delay-rate offset. Next, the fringes of J1755−2232 were searched using the station-based delay/rate solution determined with a fringe-finder, and an image of J1755−2232 was obtained using self-calibration and CLEAN algorithms.

The absolute position of the maser source was obtained by applying the phase solutions of J1755−2232 to the maser source (phase-referencing method). Doppler tracking was carried out on the maser source. Finally, we produced images of 10–20 individual velocity channels to search for maser spots. The channels used cover the LSR velocities of the maser features detected in scalar averaged spectra of each epoch: from between −15 and −18 km s^{-1} to between −13 and −18 km s^{-1}.

Each of the velocity channels was imaged with a field of view of $2'' \times 2''$ with 1024×1024 grids by CLEAN with a threshold of a signal-to-noise ratio of 4.5 (4.5σ detection limit). Each detected maser spot was imaged with 10 mas $\times$ 10 mas and 256×256 grids (0.04 mas pixel^{-1}).

After the imaging process, we conducted astrometric analysis using the result of phase-referenced analysis.

4 Results

Figure 1 shows the total-power spectrum of the H_2O maser emission toward G7.47+0.06 in the Mizusawa station on 2011/045. Around the systemic velocity of $v_{sys} = -13.9$ km s^{-1}, there are a strong peak and a weak one the LSR velocities of which are −15.90 km s^{-1} and −13.16 km s^{-1}, respectively. Figure 2 shows the scalar-averaged cross-power spectrum using the Mizusawa–Ogasawara baseline on 2009/062. The feature that is blueshifted by 1–3 km s^{-1} from v_{sys} is detected at almost all epochs; however, the weak feature of −13.16 km s^{-1} shown in figure 1 is never detected in scalar-averaged cross-power spectra.

Table 2 lists all the detected maser features throughout all the epochs. To obtain each feature, we calculated the
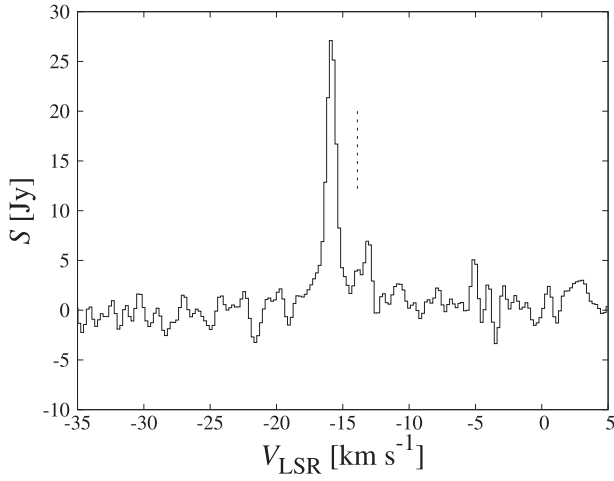
Fig. 1. Total-power spectrum of H_2O maser emission toward G7.47+0.06 in the Mizusawa station on 2011/045. The spectrum is integrated over 600 s. A dashed line indicates a systemic velocity of $-13.9\,\mathrm{km\,s^{-1}}$ (Bronfman et al. 1996).
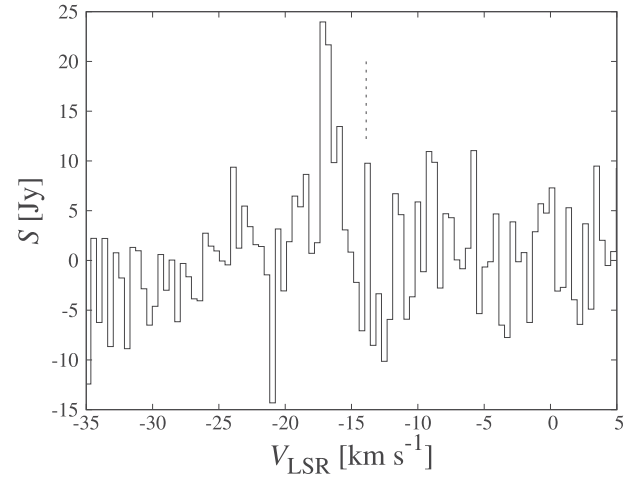

Fig. 2. Scalar-averaged cross-power spectrum of H_2O maser emission toward G7.47+0.06 obtained using VERA on 2009/062. The spectrum is integrated over 900 s on the Mizusawa–Ogasawara baseline. A dashed line indicates a systemic velocity of $-13.9\,\mathrm{km\,s^{-1}}$ (Bronfman et al. 1996).

weighted average of velocity, position, and flux density of detected spots at some continuous channels detecting maser spots. In total, we detected 20 maser features whose LSR velocities ranged from $-17.2\,\mathrm{km\,s^{-1}}$ to $-13.7\,\mathrm{km\,s^{-1}}$. The SNRs of maser features were 23–158 and the thermal noise limited positional errors given by $0.5(\theta_{\mathrm{beam}}/\mathrm{SNR})$ were 0.01–0.06 mas, where θ_{beam} was θ_{maj} or θ_{min} in table 1. Maser features were not detected because of the poor

sensitivities due to the bad weather at several stations on 2010/068, 2010/297, and 2011/255. On the other hand, maser features were not detected because of low-flux densities of masers on 2010/356 and 2011/355. The velocities are also near to the velocities of $v_{\mathrm{LSR}} = -14.0\,\mathrm{km\,s^{-1}}$ (H_2CO absorption, Downes et al. 1980) and $-14.5\,\mathrm{km\,s^{-1}}$ (OH absorption, Wouterloot et al. 1993). Features 1–4 in table 2 are named in order that blueshift is large.

Table 2. Detected maser features of G7.47+0.06.*

Epoch	Feature ID	v_{LSR} $(\mathrm{km\,s^{-1}})$	RA offset (mas)	Dec offset (mas)	S $(\mathrm{Jy\,beam^{-1}})$
2009/062	1	−17.04	49.50	2.72	3.78
	2	−16.32	45.62	−1.87	1.69
	3	−15.90	54.26	4.39	2.73
2009/136	1	−16.79	48.63	1.92	6.29
	2	−16.03	44.48	−2.50	3.72
	3	−15.66	53.36	3.65	4.13
2009/239	1	−16.63	48.52	0.41	4.02
2010/009	1	−16.83	47.25	−1.45	3.89
	2	−16.11	43.22	−6.02	3.61
	3	−15.61	52.06	0.26	4.00
	4	−13.69	101.08	−50.51	2.22
2010/151	1	−16.97	46.65	−2.62	2.84
	2	−16.32	42.46	−7.46	5.21
	3	−15.82	51.44	−0.78	4.39
	4	−14.09	100.38	−51.82	1.78
2011/128	1	−17.16	44.20	−7.03	3.10
	2	−16.16	39.99	−11.70	4.97
	3	−15.87	49.04	−5.31	4.11
2011/255	2	−16.37	38.63	−13.05	4.75
	3	−15.48	47.49	−6.05	1.81

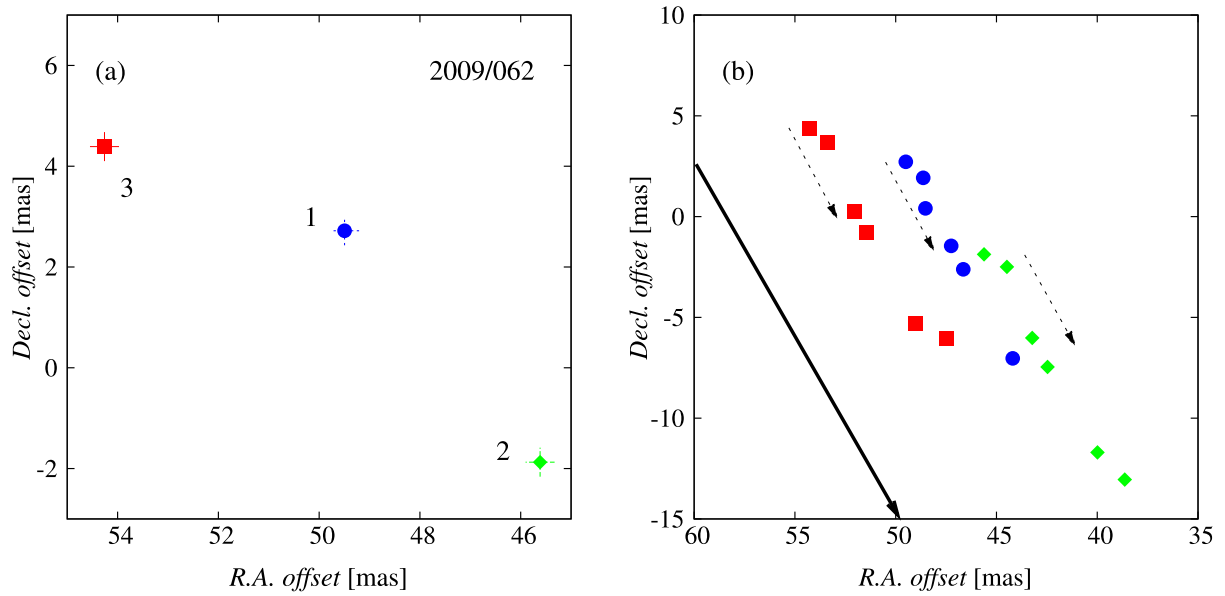*Position errors of all features are 0.29 mas as the result of parallax fit.

Fig. 3. (a) Distribution of maser features on 2009/062. The delay tracking center position (0,0) corresponds to $\alpha_{\text{J2000.0}} = 18^h02^m13^s179$, $\delta_{\text{J2000.0}} = -22°27'58''96$. Numbers indicate feature ID (see table 2). Position errors of all features are 0.29 mas as the result of parallax fit. (b) Distribution of maser features throughout all epochs. Thin dashed arrows indicate proper motions per year of individual maser features. A thick arrow is parallel to the Galactic plane, and its head points to the Galactic center. (Color online)

Feature 4 has the nearest velocity to v_{sys}. These features, located around $(\Delta\text{RA}, \Delta\text{Dec}) \approx (101\,\text{mas}, -51\,\text{mas})$, are detected in only two epochs (2010/009 and 2010/151); therefore, it is difficult to trace the motion of feature 4.

Figure 3a shows a map of features 1 to 3; however, we plot the position error as the result of parallax fit (see subsection 4.1) in this figure. The maser features are distributed in an area of 10 mas × 10 mas. Figure 3b shows the movement of these three features. The features move from the north-east to the south-west and are approaching the Galactic center parallel to the Galactic plane.

4.1 Annual parallax

We used three maser features to measure the parallax. The least-squares method was used for fitting the movement of each maser feature throughout the observing epochs to obtain a sinusoidal parallax curve and a linear proper motion represented by the following equations (Green 1985):

$$\alpha = \alpha_0 + \mu_\alpha t + \pi F_\alpha, \tag{1}$$

$$\delta = \delta_0 + \mu_\delta t + \pi F_\delta, \tag{2}$$

where (α_0, δ_0) are the coodinates at $t = 0$ (2009 Jan 0), and π is the annual parallax; (F_α, F_δ) are sinusoidal functions of direction and time describing a parallax ellipse, and (μ_α, μ_δ) are proper motions in RA and Dec, respectively; t is the time elapsed from the origin of epoch.

We conducted a combined parallax fit, in which the positions of three features were fitted simultaneously with one common parallax, but three different proper motions and position offsets. In the fitting process, we obtained systematic errors (post-fit residuals) of 0.284 mas in the RA direction, and of 0.279 mas in the Dec direction, which were added to make the reduced χ^2 so as to be approximately unity. These post-fit residuals are larger than the thermal noise limited errors and appropriate compared with the residuals of other VERA observations (e.g., Motogi et al. 2011). As reported previously in Honma et al. (2007), it is difficult to estimate the individual error sources in the VLBI astrometry quantitatively. We therefore adopted the post-fit residuals for the positional errors of the maser features. As a result of this fit, we obtain an annual parallax of 0.170 ± 0.135 mas, corresponding to a distance of $5.88^{+22.44}_{-2.60}$ kpc. The large error (79.2%) of the parallax indicates that the parallax is poorly constrained. It is difficult to obtain the distance from our data via the annual parallax. Figure 4a shows the time variation of RA and Dec offsets with the proper motions subtracted, but the model curve cannot be fitted to the observed data well.

We show proper motions as the results of parallax fitting in table 3. The proper motions in the case of given $\pi = 0$ are also shown for comparison; see also figure 4b. Both results are consistent within the 1σ errors. Therefore, there is no significant difference in proper motions regardless of whether the parallax fit is included or not.
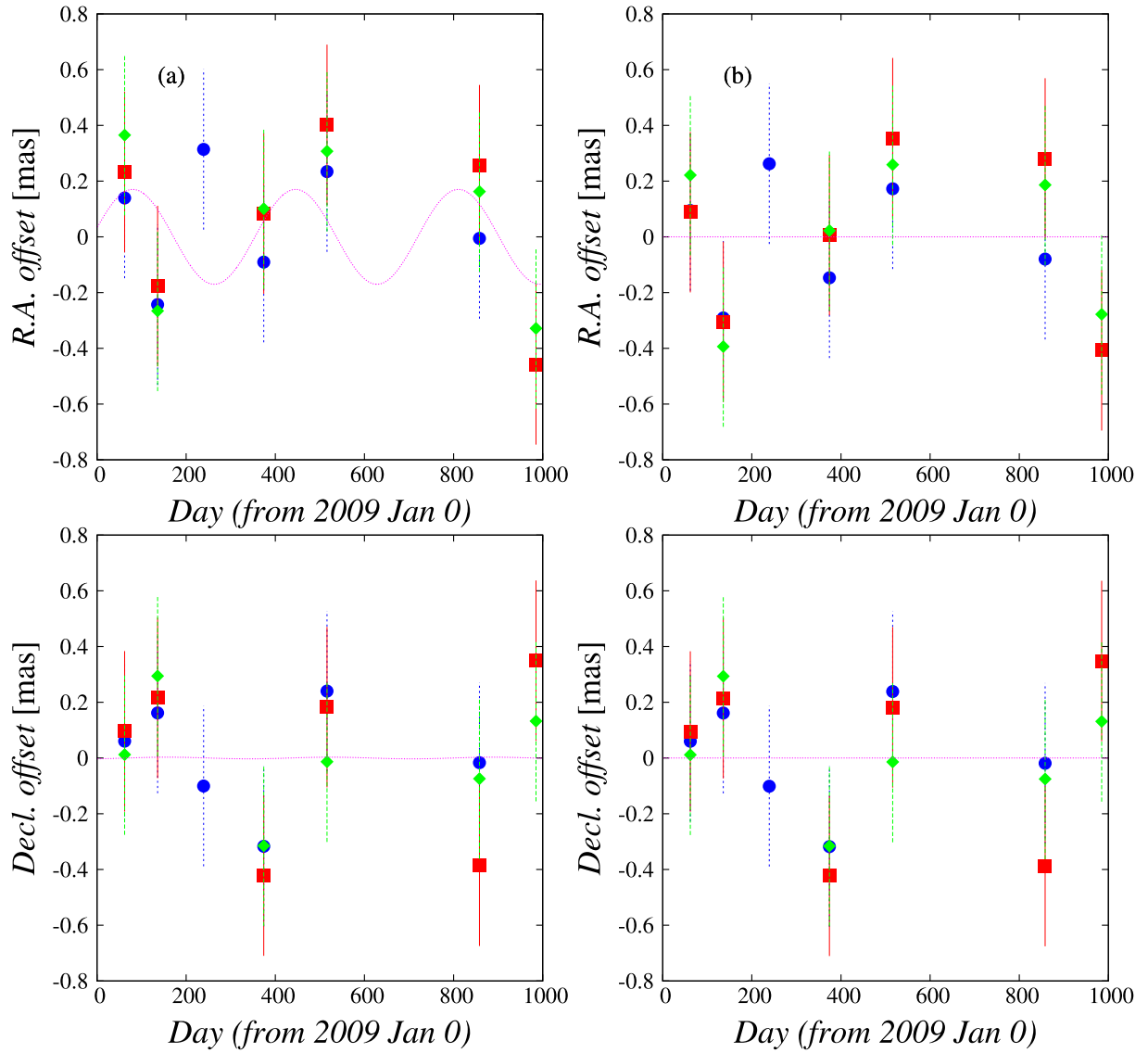
Fig. 4. Time variation of RA (top) and Dec (bottom) offsets with the proper motions subtracted. Blue circles, green diamonds, and red squares correspond to features 1 to 3 in figure 3, respectively. Position errors of all features are 0.29 mas as the result of parallax fit. (a) Curves indicate the best-fitting models for annual parallax. As the result of this fit, $\pi = 0.170 \pm 0.135$ mas. (b) The case of $\pi = 0$ mas. (Color online)

Table 3. Absolute proper motions in RA and Dec directions.

Feature ID	Proper motion (mas yr^{-1})*			
	$\pi = 0.170$ mas		$\pi = 0$ mas (linear)[†]	
	RA	Dec	RA	Dec
1	-2.37 ± 0.17	-4.44 ± 0.17	-2.35 ± 0.16	-4.44 ± 0.16
2	-2.49 ± 0.14	-4.47 ± 0.13	-2.57 ± 0.13	-4.47 ± 0.13
3	-2.41 ± 0.14	-4.23 ± 0.13	-2.48 ± 0.13	-4.23 ± 0.18
Average[‡]	-2.42 ± 0.09	-4.39 ± 0.08	-2.46 ± 0.08	-4.38 ± 0.08

*Results of parallax fitting. Each error indicates 1σ.

[†]We give $\pi = 0$ mas to fit linearly.

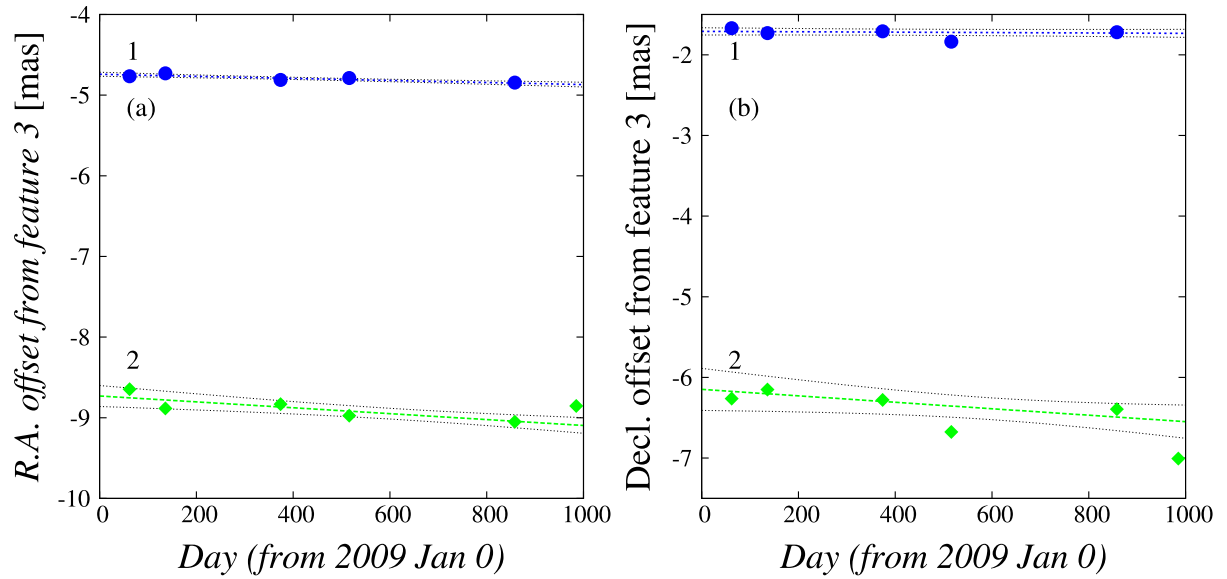[‡]Weighted average of the three features.

Fig. 5. Internal proper motion. (a) and (b) show time variations of the relative positional offsets of features 1 and 2 with respect to feature 3 in RA and Dec directions, respectively. Numbers indicate feature ID. Position errors of all features are given by propagation of the thermal-noise-limited positional errors, but too short to plot: the maximum of the errors is 0.05 mas. Thick straight lines indicate the results of weighted least-squares linear fitting (see table 4). Thin curves show the 1σ confidence band of the fitting results. (Color online)

Table 4. Internal proper motions in RA and Dec directions.

Feature ID	Proper motion (mas yr^{-1})*	
	RA	Dec
1	-0.05 ± 0.02	-0.01 ± 0.02
2	-0.13 ± 0.05	-0.15 ± 0.08

*Relative motion to feature 3. Each error indicates 1σ.

4.2 Internal proper motion

Figures 5a and 5b show time variation of the relative positional offsets of features 1 and 2 with respect to feature 3 in RA and Dec directions, respectively. Features 2 and 3 are detected at six epochs, and feature 1 is detected at five epochs excluding 2011/255. Position errors given by propagation of the thermal-noise-limited positional errors are 0.01–0.02 mas excluding 2010/151 (Dec only) and 2011/255 (RA and Dec): Mizusawa station did not participate on 2010/151, and the weather conditions on 2011/255 were bad. Results of a weighted least-squares linear fitting are listed in table 4. Internal proper motions are from -0.01 to -0.15 mas yr^{-1}, which corresponds to a range of from -1 to -14 km s^{-1} in the case of D (source distance) = 20 kpc. The time variations of the relative positional offsets are less than 3σ of those fitting errors. Therefore, no significant internal proper motion is detected.

4.3 Absolute proper motions in l and b directions

Figure 6 shows the position variation of features 1–3 along galactic longitude (l) and galactic latitude (b). Because we did not detect the annual parallax from our data, we fitted a straight line to all the data of each feature using a least-squares fitting. The results of the fitting are listed in table 5. When we use the position errors as the result of the parallax fit, the fitting becomes unweighted because all the features have the same errors. We obtain proper motions of -5.03 ± 0.07 mas yr^{-1} along galactic longitude and -0.01 ± 0.09 mas yr^{-1} along galactic latitude, based on the weighted average of three features. We detect significant motion toward $l = 0°$ along the Galactic plane. However, in the direction perpendicular to the Galactic plane, the motions are 1σ or less than those fitting errors. Therefore, all features move almost parallel to the Galactic plane.

5 Discussion

5.1 Distance measurement

In this subsection, we explain a method to measure distance using an absolute proper motion.

We assume the following: (1) all stars in the Galaxy are on the same plane (the Galactic plane), and (2) the rotation of all stars around the Galactic center is purely circular. When the galactic longitude of a target star is l, as shown in figure 7, the distance between the star and the Galactic
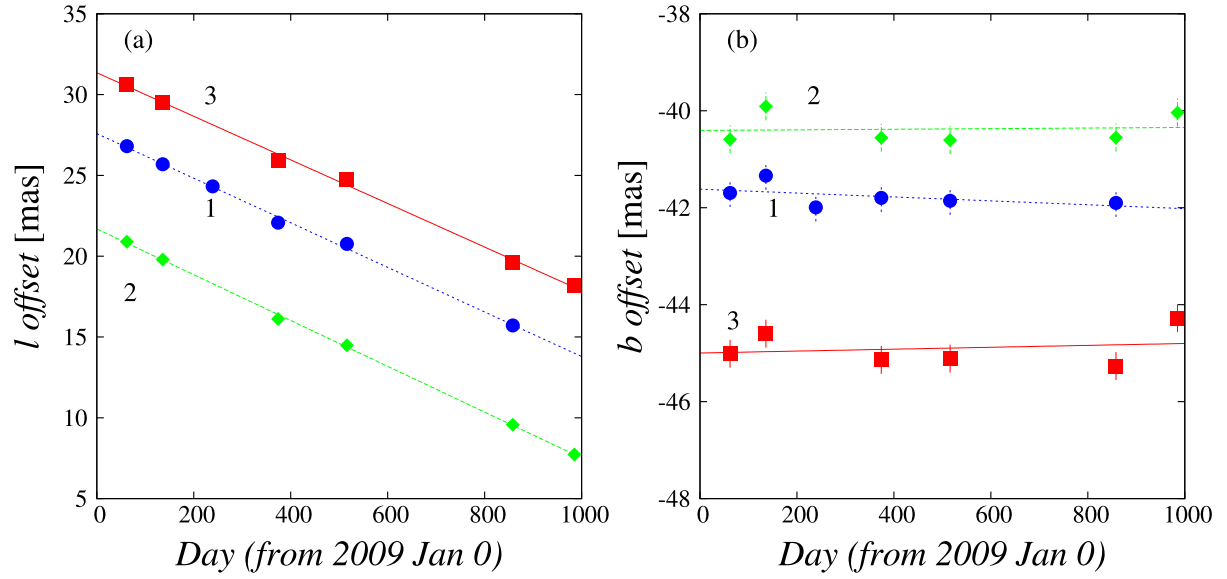
Fig. 6. Time variations of the positions of features 1 to 3 along (a) galactic longitude and (b) galactic latitude. The abscissa indicates days from 2009 Jan 0, and the ordinate indicates the offset from the reference position; the reference position corresponds to $l = 7°.47065$, $b = 0°.05845$. Numbers indicate feature ID. Position errors of all features are 0.29 mas as the result of parallax fit. Straight lines indicate the results of unweighted least-squares linear fitting (see table 5). (Color online)

Table 5. Absolute proper motions in l and b directions.

Feature ID	Proper motion (mas yr^{-1})*	
	l	b
1	-5.04 ± 0.13	-0.15 ± 0.12
2	-5.18 ± 0.07	$+0.02 \pm 0.15$
3	-4.93 ± 0.12	$+0.07 \pm 0.18$
Average†	-5.03 ± 0.07	-0.01 ± 0.09

*Each error indicates 1σ.
†Weighted average of the three features.

center, R, is given by

$$R = \sqrt{D^2 + R_0^2 - 2DR_0 \cos l} \qquad (3)$$

where R_0 is the distance between the Galaxy center and the LSR, and D the distance between the target star and the LSR. Rotation velocities of the LSR and the star are Θ_0 and Θ, respectively. A component of Θ perpendicular to the line-of-sight is the following:

$$\Theta \cos \phi = \Theta \frac{R_0 \cos l - D}{\sqrt{D^2 + R_0^2 - 2DR_0 \cos l}}, \qquad (4)$$

where ϕ is the angle opposite R_0 in figure 7. Considering the component of Θ_0 perpendicular to the line-of-sight, the tangential velocity of the star is

$$V_t = \Theta \frac{R_0 \cos l - D}{\sqrt{D^2 + R_0^2 - 2DR_0 \cos l}} - \Theta_0 \cos l. \qquad (5)$$

Therefore, the proper motion of the star along the l direction under the galactic rotation, $\mu = V_t/D$, is given as a function
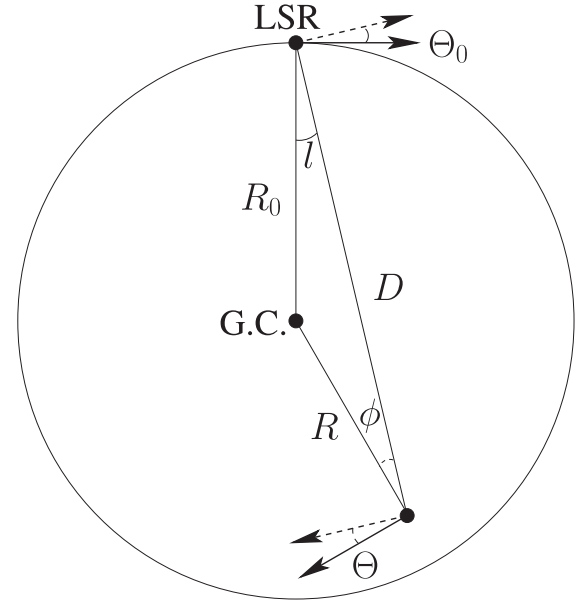

Fig. 7. Schematic view of G7.47+0.06. "G.C." means the Galactic center. Θ_0 and Θ are the rotation velocities of the LSR and a star (G7.47+0.06), respectively (solid arrows). Dashed arrows indicate the components of the rotation velocities perpendicular to the line-of-sight. R_0, R, and D are the distances between the G.C. and the LSR, between the G.C. and the star, and between the LSR and the star, respectively. l and ϕ indicate angles of the G.C.–LSR–star and the G.C.–star–LSR, respectively.

of D, if Θ_0, R_0, and l are known. Θ is given assuming a Galactic rotation curve. In the same way, the radial velocity of the star is obtained by

$$V_r = \Theta \frac{R_0 \sin l}{\sqrt{D^2 + R_0^2 - 2DR_0 \cos l}} - \Theta_0 \sin l. \qquad (6)$$
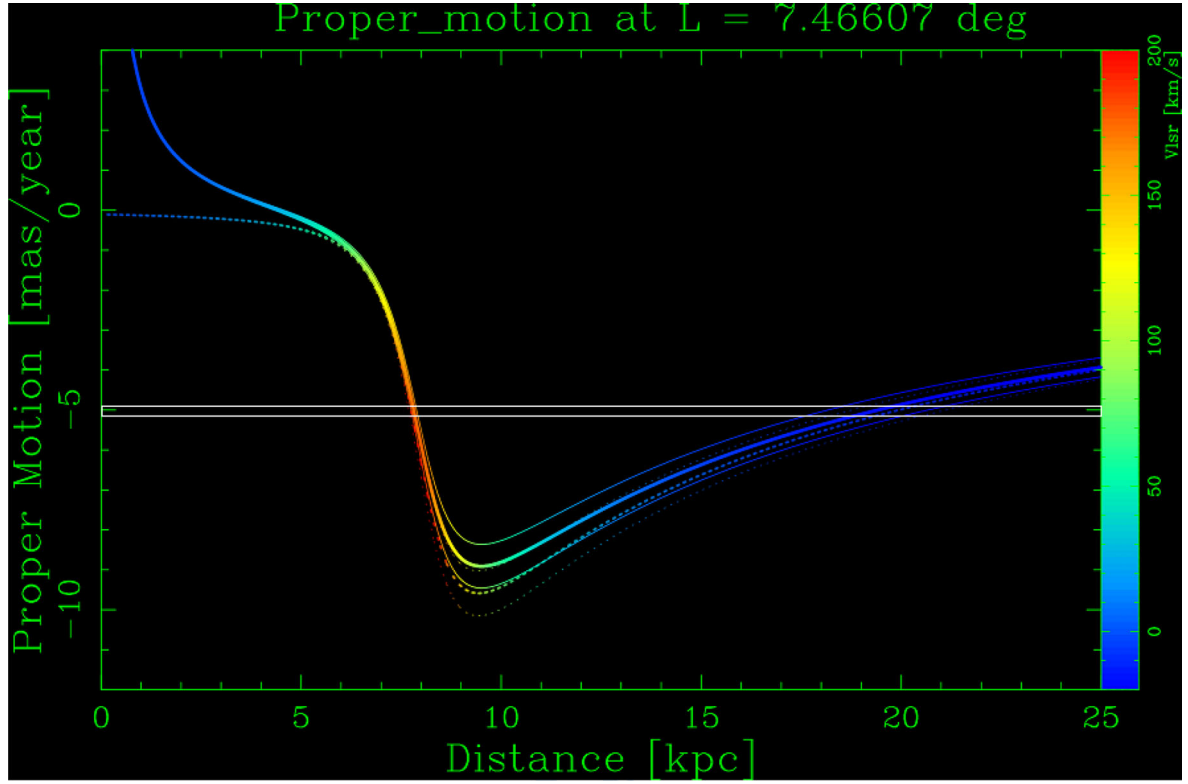
Fig. 8. Proper motion as a function of distance, in the case of $l = 7°.47$, $R_0 = 8.05$ kpc. The color scale indicates line-of-sight velocity. Three dashed curves indicate the distances from the LSR in the cases of $\Theta = \Theta_0 = 224, 238$, and $252\,\mathrm{km\,s^{-1}}$ from above, respectively. Solid curves indicate the distance from the Sun in the case of $\Theta = \Theta_0 (R/R_0)^\alpha$ and $\alpha = 0.05$. Three solid curves correspond to the cases of $\Theta_0 = 224, 238$, and $252\,\mathrm{km\,s^{-1}}$ from above, respectively. The white-bound rectangle is an area corresponding to $\mu = -5.03 \pm 0.07\,\mathrm{mas\,yr^{-1}}$.

Sofue (2011) discussed the accuracy of kinematical distances determined by a radial-velocity method and a proper-motion method. In the radial-velocity method, the distance error is the largest along the line passing through the Sun and the Galactic center (the Sun–GC line), where the motion by galactic rotation is perpendicular to the line of sight. By contrast, in the proper-motion method, the distance ambiguity is drastically reduced in the region beyond the Galactic center near the Sun–GC line. Equation (27) in Sofue (2011) gives the error in the distance derived from the proper-motion method:

$$\Delta D_\mu$$
$$= \frac{D^2 \delta\mu}{\Theta[D(D - R_0 \cos l)^2 / R^3 - (2D - R_0 \cos l)/R] - \Theta_0 \cos l}. \tag{7}$$

This error depends on the error of the proper motion μ.

In this paper, we adopt $R_0 = 8.05 \pm 0.45$ kpc and $\Theta_0 = 238 \pm 14\,\mathrm{km\,s^{-1}}$ (Honma et al. 2012). As concerns a rotation curve, we use the same power-law model as Honma et al. (2012). In the power-law model of the rotation curve, the Galactic rotation velocity at any radius R is assumed to

obey the following rotation law:

$$\Theta(R) = \Theta_0 \left(\frac{R}{R_0}\right)^\alpha, \tag{8}$$

where α is the rotation curve index. When $\alpha = 0$, the rotation is flat. Honma et al. (2012) derived $\alpha = 0.022 \pm 0.029$ from analyses to determine the fundamental parameters of the Galaxy based on VLBI astrometry. We apply the flat case of $\alpha = 0$ and the maximum case of $\alpha = 0.05$, and then we add the solar peculiar motion to both of the cases.

First we consider the flat case of $\alpha = 0$; i.e., we assume $\Theta_0 = \Theta = 238 \pm 14\,\mathrm{km\,s^{-1}}$. Figure 8 shows the proper motion μ as a function of the distance D, in the case of $l = 7°.47$. Three dashed curves indicate the cases of $\Theta_0 = \Theta = 224, 238$, and $252\,\mathrm{km\,s^{-1}}$ from above, respectively. The white-bound rectangle is an area corresponding to $\mu = -5.03 \pm 0.07\,\mathrm{mas\,yr^{-1}}$. The rectangle intersects the curves at two points: $D \approx 7.6$ and 19.8 kpc. If the distance of G7.47+0.06 is $D \approx 7.6$ kpc, the radial velocity is over $200\,\mathrm{km\,s^{-1}}$, as shown in figure 8. Therefore, we can exclude the possibility of $D \approx 7.6$ kpc.

Substituting $D = 19.8$ kpc, $\delta\mu = 0.07\,\mathrm{mas\,yr^{-1}}$, and $\Theta_0 = \Theta = 238\,\mathrm{km\,s^{-1}}$ in equation (7), the distance error

Table 6. Distance error estimation.

Case	α^*	$U_\odot, V_\odot, W_\odot$ (km s^{-1})	R_0 (kpc)	Θ_0 (km s^{-1})	μ (mas)	D (kpc)
	0	–	8.05 ± 0.45	238	-5.03	19.8 ± 0.1
	0	–	8.05	238 ± 14	-5.03	19.8 ± 1.2
	0	–	8.05	238	-5.03 ± 0.07	19.8 ± 0.3
(1)	0	–	8.05 ± 0.45	238 ± 14	-5.03 ± 0.07	19.8 ± 1.5
(2)	0.05	–	8.05 ± 0.45	238 ± 14	-5.03 ± 0.07	20.1 ± 1.6
(3)	0	$(11.1, 12.2, 7.3)^\dagger$	8.05 ± 0.45	238 ± 14	-5.03 ± 0.07	19.3 ± 1.5
(4)	0.05	$(11.1, 12.2, 7.3)^\dagger$	8.05 ± 0.45	238 ± 14	-5.03 ± 0.07	19.5 ± 1.6

$^*\Theta(R) = \Theta_0(R/R_0)^\alpha$.

†Schönrich, Binney, and Dehnen (2010).

becomes $\Delta D_\mu = 0.1$ kpc. This error is very small. The distance error practically depends on the uncertainty of the rotation curve models rather than the proper motion error.

Now we estimate the error of D. The three rows from the top of table 6 show the effect of the individual errors of R_0, Θ_0, and μ: $R_0 = 8.05 \pm 0.45$ kpc, $\Theta_0 = 238 \pm 14$ km s^{-1}, and $\mu = -5.03 \pm 0.07$ mas yr^{-1}. It is found that the error in Θ_0 has the greatest impact. Taking into account all errors of R_0, Θ_0, and μ, we obtain the distance of $D = 19.8 \pm 1.5$ kpc with accuracy of 7.5% uncertainty [case (1) in table 6]. The maximum (minimum) distance corresponds to the case of $R_0 = 7.60\,(8.50)$ kpc, $\Theta_0 = \Theta = 252\,(224)$ km s^{-1}, and $\mu = -4.96\,(-5.10)$ mas yr^{-1}.

Secondly, we change the rotation curve index. In the maximum case of $\alpha = 0.05$ [case (2) in table 6], we obtain the distance of $D = 20.1 \pm 1.6$ kpc with an accuracy of 8.1% uncertainty, in the same way as the case of flat rotation. Due to the difference of α, the distance becomes far 0.3 kpc than the distance of case (1) by 0.3 kpc and the error becomes a little larger.

Thirdly, we add the solar peculiar motion to case (1) [case (3) in table 6]. In this case, D is the distance not from the LSR, but from the Sun. We adopt the solar motion based on a traditional definition of $(U_\odot, V_\odot, W_\odot) = (11.1, 12.2, 7.3)$ km s^{-1}, where $U_\odot$ is the solar motion toward the Galactic center, $V_\odot$ the solar motion toward $l = 90°$, and $W_\odot$ the solar motion toward the north Galactic pole (Schönrich et al. 2010). We obtain the distance of $D = 19.3 \pm 1.5$ kpc with an accuracy of 7.7% uncertainty. With the addition of the solar peculiar motion, the distance is closer 0.5 kpc than the distance of case (1) by 0.5 kpc and the error do not change.

Lastly, we add the solar peculiar motion to case (2) [case (4) in table 6]. Three solid curves in figure 8 correspond to this case: $\Theta_0 = 224, 238$, and 252 km s^{-1} from above, respectively. We obtain the distance of $D = 19.5 \pm 1.6$ kpc with an accuracy of 8.3% uncertainty. With the addition of the solar peculiar motion, the distance is closer 0.6 kpc

than the distance of case (2) by 0.6 kpc and the error do not change. The solar peculiar motion has a small influence on distance measurement on the far side of the Galactic center, although it has a significant influence on the near side as shown in figure 8.

Considering the four cases, we conservatively conclude that the source distance is 20 ± 2 kpc. In spite of the difference of a rotation curve index and the solar peculiar motion, the accuracy is at a 10% level. This distance indicates that G7.47+0.06 is in the Scutum-Centaurus arm.

[After Honma et al. (2012), Reid et al. (2014) estimated the Galactic parameters, $R_0 = 8.34 \pm 0.16$ kpc and $\Theta_0 = 240 \pm 8$ km s^{-1}. When we use these R_0 and Θ values, the distances of cases (1) to (4) become the following: (1) 20.0 ± 1.0 kpc, (2) 20.2 ± 1.0 kpc, (3) 19.4 ± 1.0 kpc, and (4) 19.6 ± 1.0 kpc. As a result, the distance of $D = 20 \pm 2$ kpc is obtained.]

Some papers report on the kinematic distances to G7.47+0.06. Downes et al. (1980) measured a kinematic distance of 27 ± 5 kpc using a radial velocity of the H110α recombination line, -17.0 km s^{-1}; the distance became 22 ± 4 kpc when scaled from $R_0 = 10$ kpc to 8.05 kpc. Wink, Altenhoff, and Mezger (1982) observed the H76α recombination line and derived a kinematic distance of $25.1^{+10.8}_{-4.2}$ kpc from a radial velocity of -13.0 km s^{-1} ($20.2^{+8.7}_{-3.4}$ kpc scaled to $R_0 = 8.05$ kpc). Scaling from $R_0 = 8.5$ kpc to 8.05 kpc, kinematic distances calculated by Palagi et al. (1993) (29.37 kpc, -16.6 km s^{-1} at H$_2$O maser), Peeters et al. (2002) [3.0 or 13.8 kpc, $+15.4$ km s^{-1} at CS(2–1)], and Balser et al. (2011) (30.3 kpc, -16.93 km s^{-1} at H87α–H93α recombination line) became 27.81 kpc, 2.8 or 13.1 kpc, and 28.7 kpc, respectively. A kinematic distance varies depending on the radial velocity of the observed line. A hydrogen recombination line has a large line width of a few tens km s^{-1}; therefore the obtained distance includes a large error. The distances by Downes et al. (1980) and Wink, Altenhoff, and Mezger (1982) are consistent with our

distance because of those large errors. Because Balser et al. ([2011](#)) did not report on the error of their distance, we do not know whether their and our distances are consistent within the errors. Palagi et al. ([1993](#)) used the radial velocity of an H_2O maser emission. However, because the H_2O maser features are located in the outflow from a center star, the radial velocity may be shifted by a few tens of kilometres per second from the systemic velocity. Although Peeters et al. ([2002](#)) adopted the velocity of CS(2–1) line by Bronfman, Nyman, and May ([1996](#)), they did not use the systemic velocity of $-13.9 \, \mathrm{km \, s^{-1}}$ but $+15.4 \, \mathrm{km \, s^{-1}}$. Their distance is nearer than the other distances. The velocities of $+15.4 \, \mathrm{km \, s^{-1}}$ are near the velocities of molecular absorption lines, $+15.0 \, \mathrm{km \, s^{-1}}$ (H_2CO absorption, Downes et al. [1980](#)) and $+15.6 \, \mathrm{km \, s^{-1}}$ (OH absorption, Wouterloot et al. [1993](#)). There may be another cloud in front of G7.47+0.06.

The distance measurement depending on the proper motion has a small influence on the velocity shift of a target. If Θ in equation (5) shifts by $\pm 10 \, \mathrm{km \, s^{-1}}$, μ changes by $\pm 0.1 \, \mathrm{mas \, yr^{-1}}$; the proper motion error corresponds to the distance error of $\pm 0.4 \, \mathrm{kpc}$ of each rotation curve. Therefore, if the maser features move in the outflow, the distance measured from the proper motion has a small error.

5.2 Physical parameter estimation

G7.47+0.06 was mapped at 1.5, 4.9, and 15.0 GHz using the Very Large Array of the National Radio Astronomy Observatory (Garay et al. [1993](#)). Garay et al. ([1993](#)) detected complex sources, A, B, C1, C2, and C3. All components are located in the region with a diameter of $\sim$1 min. Garay et al. ([1993](#)) estimated physical parameters of components adopting $D = 6.3 \, \mathrm{kpc}$; the diameters of $d = 0.08$–$0.3 \, \mathrm{pc}$, the electron densities of $N_e = 1.5 \times 10^3$–$1.8 \times 10^4 \, \mathrm{cm^{-3}}$, and so on. The spectral types of the sources are O8–O9.5. Adopting our distance of $D = 20 \, \mathrm{kpc}$, scaled physical parameters are $d = 0.25$–$0.89 \, \mathrm{pc}$, $N_e = 8.4 \times 10^2$–$1.0 \times 10^4 \, \mathrm{cm^{-3}}$; these electron densities correspond to the density of a UC H II region. The spectral types become O5.5–O6.5. The size of the region of $\sim$1 min, including A–C3, corresponds to $\sim$6 pc, which is comparable with the size of an open cluster. The H_2O maser features are near the brightest component C1 with the spectral type O5.5 and were detected stably for more than two years. The features have probably been associated with a high-mass star within C1.

6 Summary

H_2O maser emission from a UC H II region G7.47+0.06 was observed with VLBI. The results are summarized as follows.

1. H_2O maser features blueshifted by 1–3 $\mathrm{km \, s^{-1}}$ from the systemic velocity were detected in almost all epochs. Three maser features move parallel to the Galactic plane and are approaching the Galactic center.

2. We conducted a parallax fit in the three features, but the obtained parallax has a very large error. It is difficult to measure the annual parallax distance to G7.47+0.06 accurately.

3. Significant internal proper motion is not detected. Absolute proper motions are $\mu = -5.03 \pm 0.07 \, \mathrm{mas \, yr^{-1}}$ and $-0.01 \pm 0.09 \, \mathrm{mas \, yr^{-1}}$ in l and b directions, respectively, averaging the results of an unweighted linear least-squares fit to the three features.

4. From the relation between the distance from the Sun to a star and its absolute proper motion, we derived $D = 20 \pm 2 \, \mathrm{kpc}$ with accuracy of 10% uncertainty.

5. The physical parameters of the H II region estimated by Garay et al. ([1993](#)) were scaled from $D = 6.3 \, \mathrm{kpc}$ to 20 kpc. The H_2O maser features are associated with a massive star-forming region corresponding to the spectral type of O5.5.

References

Balser, D. S., Rood, R. T., Bania, T. M., & Anderson, L. D. 2011, ApJ, 738, 27

Bronfman, L., Nyman, L.-A., & May, J. 1996, A&AS, 115, 81

Chikada, Y., et al. 1991, in Frontiers of VLBI, ed. H. Hirabayashi et al. (Tokyo: Universal Academy Press), 79

Comoretto, G., et al. 1990, A&AS, 84, 179

Downes, D., Wilson, T. L., Bieging, J., & Wink, J. 1980, A&AS, 40, 379

Garay, G., Rodriguez, L. F., Moran, J. M., & Churchwell, E. 1993, ApJ, 418, 368

Green, R. M. 1985, Spherical Astronomy (Cambridge: Cambridge University Press), 339

Honma, M., et al. 2007, PASJ, 59, 889

Honma, M., et al. 2008, PASJ, 60, 935

Honma, M., et al. 2012, PASJ, 64, 136

Honma, M., Kawaguchi, N., & Sasao, T. 2000, Proc. SPIE, 4015, 624

Iguchi, S., Kurayama, T., Kawaguchi, N., & Kawakami, K. 2005, PASJ, 57, 259

Kawaguchi, N., Sasao, T., & Manabe, S. 2000, Proc. SPIE, 4015, 544

Kobayashi, H., et al. 2008, in Proc. IAU Symp. 248, A Giant Step: from Milli- to Micro-arcsecond Astrometry, ed. W. J. Jin et al. (Cambridge: Cambridge University Press), 148

Motogi, K, Sorai, K, Habe, A, Honma, M, Kobayashi, H, & Sato, K. 2011, PASJ, 63, 31

Nagai, H., et al. 2013, PASJ, 65, 24

Palagi, F., Cesaroni, R., Comoretto, G., Felli, M., & Natale, V. 1993, A&A, 101, 153

Peeters, E., et al. 2002, A&A, 381, 571

Petrov, L., Hirota, T., Honma, M., Shibata, K. M., Jike, T., & Kobayashi, H. 2007, AJ, 133, 2487

Reid, M. J., et al. 2014, ApJ, 783, 130

Schönrich, R., Binney, J., & Dehnen, W. 2010, MNRAS, 403, 1829

Sofue, Y. 2011, PASJ, 63, 813

Wouterloot, J. G. A, Brand, J., & Fiegle, K. 1993, A&AS, 98, 589

Wink, J. E., Altenhoff, W. J., & Mezger, P. G. 1982, A&A, 108, 227